surfaces

MDPI

Article

Engineering Porous Biochar for Electrochemical Energy Storage

Cheikh Ahmadou Bamba Diop [1,2], Déthié Faye [1], Momath Lo [1,*], Dahbia Bakiri [2,3], Huifeng Wang [2], Mohamed El Garah [4], Vaishali Sharma [5], Aman Mahajan [5], Mohamed Jouini [2], Diariatou Gningue-Sall [1] and Mohamed M. Chehimi [2,*]

[1] Laboratoire de Chimie Physique Organique et d'Analyses Environnementales (LCPOAE), Département de Chimie, Faculté des Sciences et Techniques, Université Cheikh Anta Diop, BP 5005 Dakar-Fann, Senegal; khadimbamba2742@gmail.com (C.A.B.D.); dethiefaye93@gmail.com (D.F.); diariag@ucad.edu.sn (D.G.-S.)
[2] ITODYS (UMR 7086), CNRS, Université Paris Cité, 75013 Paris, France; dahbiabakiri95@gmail.com (D.B.); hfwang178@163.com (H.W.); jouini@univ-paris-diderot.fr (M.J.)
[3] IUT de Paris-Pajol, Université Paris Cité, 75018 Paris, France
[4] LASMIS, Pôle Technologique de Sud-Champagne, Antenne de Nogent-52, 52800 Nogent, France; mohamed.el_garah@utt.fr
[5] Material Science Laboratory, Department of Physics, Guru Nanak Dev University (GNDU), Amritsar 143005, Punjab, India; sharmavaishali635@gmail.com (V.S.); aman.phy@gndu.ac.in (A.M.)
* Correspondence: momath.lo@ucad.edu.sn (M.L.); mohamed.chehimi@cnrs.fr (M.M.C.)

Abstract

In recent years, porous carbon-based materials have demonstrated their potential as electrode materials, particularly as supercapacitors for energy storage. The specific capacitance of a carbon-based material is strongly influenced by its porosity. Herein, activated biochar (BCA) from millet was prepared using $ZnCl_2$ as an activator at temperatures of 400, 700, and 900 °C. Activation was achieved through wet and dry impregnation of millet bran powder particles. The porosity of BCAs was assessed by determining the iodine and methylene blue numbers (N_I and N_{MB}, respectively), which provide information on microporosity and mesoporosity, respectively. Characterization of the BCAs was carried out using Raman spectroscopy, X-ray diffraction, X-ray photoelectron spectroscopy, and cyclic voltammetry. The data show that the BCA prepared at 700 °C following dry impregnation, P700(p), has the highest N_I and the highest geometric mean value ($\tilde{n} = \sqrt{N_I \times N_{MB}}$), a descriptor we introduce to characterize the overall porosity of the biochars. P700(p) biochar exhibited remarkable electrochemical properties and a maximum specific capacitance of 440 $F\ g^{-1}$ at a current density of 0.5 $A\ g^{-1}$, in the three-electrode configuration. This value drops to 110 $F\ g^{-1}$, in the two-electrode configuration. The high specific capacitance is not due to ZnO, but essentially to the textural properties of the biochar (represented by ñ descriptor), and possibly but to a lesser extent to small amounts of Zn_2SiO_4 left over in the biochar. Moreover, the capacitance retention increases with cycling, up to 130%, thus suggesting electrochemical activation of the biochar during the galvanostatic charge-discharge process. To sum up, the combination of pyrolysis temperature and the method of impregnation permitted to obtaining of a porous biochar with excellent electrochemical properties, meeting the requirements of supercapacitors and batteries.

Keywords: *Pennisetum glaucum*; biochar; porous materials; electrode materials; supercapacitor; capacitive retention

Academic Editors: Gaetano Granozzi, Bosi Yin and Siwen Zhang

Received: 28 September 2025
Revised: 8 November 2025
Accepted: 22 November 2025
Published: 28 November 2025

Citation: Diop, C.A.B.; Faye, D.; Lo, M.; Bakiri, D.; Wang, H.; El Garah, M.; Sharma, V.; Mahajan, A.; Jouini, M.; Gningue-Sall, D.; et al. Engineering Porous Biochar for Electrochemical Energy Storage. *Surfaces* **2025**, *8*, 87. https://doi.org/10.3390/surfaces8040087

1. Introduction

As the global population continues to grow, the rising energy demand has become an increasing concern. For decades, energy production has relied predominantly on fossil fuels, which are non-renewable and major contributors to CO_2 emissions. These harmful gases pose significant risks to both living organisms and the environment. This has motivated the development and implementation of renewable and sustainable energy sources, which are both inexhaustible and widely accessible [1,2]. In this regard, the development of systems capable of converting and conserving energy while minimizing environmental impact is essential, yet remains a significant challenge. With this in mind, supercapacitors or electrochemical capacitors, whose main aim is to store as many ions as possible in the form of charge, are the materials of choice. They are characterized by high power density and high energy density. They possess characteristics such as conductivity and porosity, as well as a large active surface area [3]. There are two primary types of supercapacitors, distinguished by their charge storage methods: electrochemical double-layer capacitors (EDLCs) and pseudocapacitors. EDLCs store energy through electrostatic interactions at the electrode–electrolyte interface, where ions from the electrolyte form an electric double layer that enables charge accumulation. Electrochemically, EDLCs are characterized by rectangular voltamograms. Pseudocapacitors store energy through reversible redox reactions between the electrolyte and electroactive species on the electrode surface, which involve electron transfer during these reactions. They exhibit rectangular voltamograms with inflection points [4,5]. The most commonly used capacitor electrode materials are made of carbon allotropes such as carbon black, fullerenes, carbon nanotubes, graphene, and carbon aerogel. They are good conductors and typically have a large surface area and surface pores, making carbon an ideal material for a capacitor [6]. However, these materials are expensive and have limitations, such as fullerene's low surface area or graphene's tendency to clump together easily, which restricts their performance.

Recently, biochar-based electrodes have attracted considerable attention due to their physicochemical properties that make them suitable for charge storage applications [7–9]. Biochars are carbon-rich materials produced through the carbonization of biomass under inert or low air conditions. The thermochemical conversion of lignocellulosic matter releases mainly H-, N-, and O-containing volatiles, resulting in a porous carbonaceous structure [10,11]. Biomass, such as agricultural wastes, is abundant and could serve as a sustainable source for producing industrial quantities of biochar, offering a cost-effective alternative to expensive carbon allotropes [12,13]. Biochars meet capacitor criteria because of their porous structure and the possibility to modify their chemical composition by adsorption, grafting, or decoration with nanoparticles [14–17]. The surface characteristics of biochar are influenced by factors such as the nature of biomass used, pyrolysis temperature, and residence time [18]. Furthermore, biochar in its natural form may exhibit limited activity due to its low porosity and smaller surface area. Activation or treatment can enhance its performance [19]. Activation of biochar mainly improves catalytic performance and increases the number of catalytic sites [20], generally manifested by a change in its surface texture [21]. However, the need for metal salt additives, which provide biochar with mechanical strength, affects the design of electrode materials and compromises electrode durability during recycling [22]. The use of $ZnCl_2$-activated biochar is investigated as a potential approach for fabricating electrodes for supercapacitors [23]. The activation process generally decreases internal resistance and promotes a uniform pore distribution throughout the matrix, thereby enhancing the material's suitability for supercapacitor applications. The areal capacitance of $ZnCl_2$-activated biochar electrodes was found to reach 342 mF cm^{-2}, which promotes the interplay of double-layer electrical capacitance/pseudocapacitance mechanisms in a matrix that favors electrolyte interactions in the pores. Micropores (ultramicropores) and mesopores are true sites of charge capture in the form of energy [24]. Similarly, some studies have shown that $ZnCl_2$ activation is a technique used in the manufacture of porous carbonaceous materials [25]. Furthermore,

$ZnCl_2$ activation significantly increased the porosity of biochar while removing volatile elements, thereby improving its energy performance. Activation with $ZnCl_2$ gives the material remarkable stability, thus maintaining a higher adsorption capacity compared to pristine biochar. Whilst BET is a traditional means to determine the specific surface area and the porous volume, the methodology based on the determination of iodine and methylene blue indices (N_I and N_{MB}, respectively) is simple and accounts for the characterization of micropores and mesopores [26–28]. This approach correlates well with the determination of the porous volume determined by nitrogen adsorption isotherm [29].

It follows that the evaluation of these indices provides data that account for the porosity of the various biochars. However, a review of the literature reveals that no studies have attempted to correlate the capacitance of biochar electrode materials with the N_I and N_{MB} descriptors.

In this study, millet bran, a waste product generated during the processing of Senegalese millet, was selected as the biomass. Millet, which is rich in minerals, is the second most consumed food in Senegal after rice. Its production was estimated at 900,000–1,000,000 tons in 2021 [9]. The biochars were prepared by co-pyrolysis of the biomass with $ZnCl_2$ as an activating agent at a mass ratio of 1:2, using both dry and wet impregnation methods.

The activated biochar samples were characterized using XRD, SEM, XPS, and Raman spectroscopy, while their porosity was evaluated with iodine and methylene blue adsorption. These biochars were employed as electrode materials and analyzed via cyclic voltammetry (CV) and electrochemical impedance spectroscopy (EIS). Subsequently, galvanostatic charge-discharge (GCD) measurements were performed to assess their suitability as supercapacitors. The results demonstrate that the specific capacitance can be both high and tunable through a combination of activation and pyrolysis temperature. Moreover, the electrochemical performance was correlated with a novel physicochemical descriptor defined as the geometric mean of the N_I and N_{MB} numbers ($\tilde{n} = \sqrt{N_I \times N_{MB}}$). To our knowledge, no such correlation has been previously reported, highlighting the significance of this study.

2. Experimental

2.1. Reagents and Instrumentation

Methylene blue ($C_{16}H_{18}ClN_3S$) $\geq$ 97%, iodine (I_2) $\geq$ 99.8%, potassium iodide (KI) $\geq$ 99.5% (Sigma-Aldrich, Berlin, Germany).

Nafion ($C_7HF_{13}O_5S.C_2F_4$) 5%, ethanol (C_2H_6O) 99% and sulfuric acid (H_2SO_4) 99% were Sigma-Aldrich products (Berlin, Germany). Millet bran residue from Senegal (Thies/Mbour) was used as the biomass feedstock.

An HR800 spectrometer with a 633 nm laser was used to produce the Raman spectrum. XRD patterns were obtained with a PANalytical diffractometer fitted with an XPERT-PRO system. The XRD data acquisition and processing were achieved with HighScore Plus software (v. 3.0.4). A K Alpha+ apparatus (Thermo) equipped with a flood gun to neutralize the static charges, and a monochromated X-ray source (Al Kα, hv = 1486.6 eV) was used for XPS measurements. The data processing was performed using Avantage software, version 6.8.0. A Hitachi SU-8030 machine was used to acquire SEM images.

Electrochemical experiments were carried out on an SP-150 Biologic potentiostat/galvanostat, fitted with EC Lab software (Seyssinet-Pariset, Paris, France). The glass cell has three electrodes: a saturated Ag/AgCl reference electrode, a graphite counter electrode, and a GC working electrode (diameter D = 3 mm and apparent surface S = 14.137 mm^2). A two-electrode configuration was also adopted for the practical aspect of specific capacitance determination.

2.2. Synthesis of Activated Biochar

The impregnation process used to obtain BCAs is represented in Figure 1. Activated millet bran biochar was obtained by dry and wet impregnation of the biochar with $ZnCl_2$ [29], at a biomass/$ZnCl_2$ mass ratio of 1 to 2. This study reveals that biochar produced with a biomass/$ZnCl_2$ mass ratio of 1:2 had a high specific surface area (S_{BET} = 1579.8 m^2 g^{-1}) compared to those made with mass ratios of 1:1. Furthermore, Zhao et al. showed that activation with $ZnCl_2$ at a pulp/$ZnCl_2$ mass ratio of 1/2 at a pyrolysis temperature of 700 °C resulted in better MB adsorption activity with a larger specific surface area [30]. The wet impregnation consists of impregnating 1 g of biomass in a beaker containing a $ZnCl_2$ solution (2 g of salt in 10 mL of water). The wet biomass powder was covered with perforated aluminum foil and left to dry at 105 °C for 24 h. The second method is dry impregnation (p), and consists in the co-pyrolysis of a mixture of 2 g of $ZnCl_2$ and 1 g of biomass. The samples were pyrolyzed at 400, 700, and 900 °C for 1 h under nitrogen. The heating rate was 20 °C min^{-1} and the nitrogen flow rate was 3 L min^{-1}. After pyrolysis, the biochars were washed with HCl (0.5 M) to remove traces of zinc chloride, metallic zinc or zinc oxide, and then with distilled water to remove chlorides. The active biochars were dried at 105 °C for 24 h.

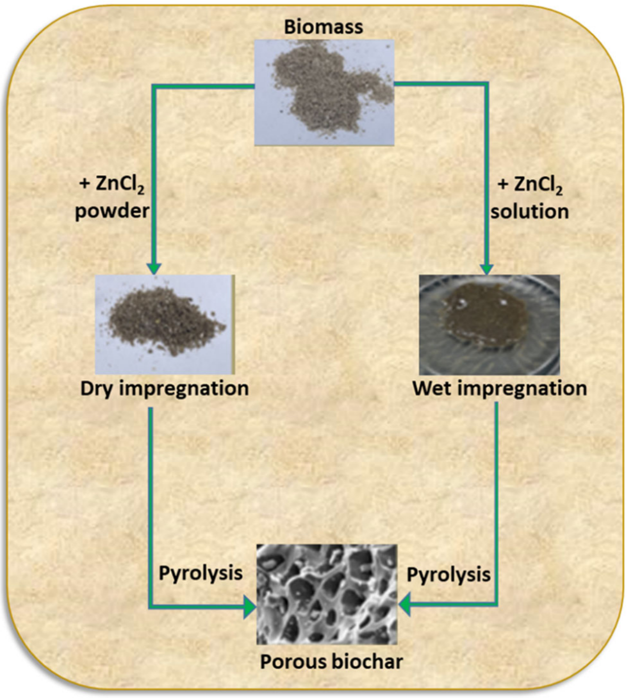

Figure 1. Wet and dry impregnation processes to make activated biochar.

2.3. Determination of Iodine and Methylene Blue Numbers

The quantity of iodine (in milligrams) absorbed is the iodine number N_I, permits to characterize the micropores of carbonaceous materials [26,31]. In brief, an iodine solution is prepared by adding 62.25 mg KI to a beaker and 31.75 mg of I_2. The mixture is stirred for 24 h in a dark place to facilitate dissolution. The dissolved solution is transferred to a 500 mL volumetric flask. 5 mg of biochar is placed in a beaker, and 10 mL of 5% hydrochloric acid is added. The mixture is boiled for 30 s, then cooled to room temperature before adding 100 mL of the prepared iodine solution and stirring for 15 min. 10 mL were pipetted with a syringe and filtered to remove the biochar, then the amount of iodine adsorbed by the biochar was determined by UV-Visible.

The methylene blue index N_{MB} represents the amount of MB consumed by 1 g of adsorbent, and permits the characterization of mesopores [26]. It is measured by preparing a stock solution of 100 mg L^{-1} of MB. This solution is diluted to yield a daughter solution of 50 mg/L. 100 mL of the daughter solution is taken and placed in a beaker containing 40 mg biochar. The mixture is stirred at 120 rpm for 1 h. The quantity of adsorbed MB is measured using the same protocol as for the iodine value.

The adsorption index N (adsorption capacity C) of iodine and methylene blue is calculated using the following equation, based on the absorption peak of iodine and methylene blue at 288 nm and 659 nm, respectively:

$$\mathrm{C} = \frac{\mathrm{C_0} - \mathrm{C_e}}{\mathrm{m}} \times \mathrm{V} \tag{1}$$

C_0: initial Concentration (mg L^{-1}), C_e: final concentration (mg L^{-1}), V: volume of aqueous solution (L) of iodine or MB and m: weight of biochars (g).

2.4. Electrochemical Properties of Biochar

The working electrode was polished, cleaned, and rinsed before any electrochemical measurements. This treatment process is as follows: alumina powder (diameter 0.05 µm) was used for abrasive polishing as the first step in preparing the glassy carbon (GC) electrode, which ensures thorough and effective regeneration of the electrode surface. To ensure there are no contaminants on the electrode surface, the second step involves immersing the electrode in a solution of 10 mL of H_2SO_4 (0.5 M) and performing cyclic voltammetry for ten cycles within a potential range of 0 to 0.8 V.

Biochar ink was prepared by dispersing 5 mg of biochar in 1 mL of ethanol containing 10 µL of Nafion and sonicating for 30 min. Then, 4 µL of the ink was drop-cast onto a polished GC electrode, air-dried for several hours [32]. After drying, the working electrode was used for electrochemical measurements. CV plots were recorded between 0 and 0.8 V/Ag/AgCl in an aqueous solution of 0.5 M sulfuric acid. CV curves were recorded in the 0–1.2 V, at a scan rate of 50 mV s^{-1} (Figure S1), for P700(p). The 0–0.8 V potential range was chosen because it ensures obtaining quasi-rectangular CV plot and is consistent with numerous other studies [23,33]. The active surface area of biochar compounds was determined using the Randles-Sevcik Equation (2) [34]:

$$I_P = (2.69 \times 10^5)\, n^{\frac{3}{2}} \times A \times D^{\frac{1}{2}} \times V^{\frac{1}{2}} \times C_0 \tag{2}$$

where I_p: anodic current, C_0: electrolyte concentration, V: scan speed, n: number of electrons transferred, and D: diffusion coefficient of the species involved. In a solution of sulfuric acid, H_2SO_4, n = 2 and $D = 1.8 \times 10^{-5}$. Typical active surface area values are reported in Table S1.

The specific capacitance (C_{Sp}, F g^{-1}) of hydro/biochar was determined from the voltammograms by using Equation (3) [35,36] and galvanostatic charge-discharge (GCD) measurements by using Equation (4). The GCD were also performed in the same potential range as the CVs, at current densities from 0.5 to 5 A g^{-1}.

Energy density E (Wh kg^{-1}) and power density P: (W kg^{-1}) are determined by Equations (5) and (6), respectively

$$C_{Sp} = \frac{\int IdV}{v \times m \times \Delta V} \tag{3}$$

$$C_{Sp} = \frac{I\Delta t}{m\Delta V} \tag{4}$$

$$E = \frac{1}{2} C_{Sp} V^2 \tag{5}$$

$$P = \frac{E}{\Delta t} \quad (6)$$

where $\int IdV$: corresponding area of the CV curve, I: the response current, V: the corresponding potential, ΔV: potential window, m: the mass of the material deposited on the surface of the electrode, Δt: discharge time (s), and v: the scan rate (mV/S).

Electrochemical impedance spectroscopy (EIS) of the biochars was also recorded in a frequency range of 0.1 Hz to 200 kHz.

3. Results and Discussion

3.1. Morphology of the Biochar Powder Particles

Figure S2 shows SEM images of BCAs obtained at different pyrolysis temperatures. The images show rough surfaces for all samples. Regardless of the impregnation method, pyrolysis at 400 °C induces fewer pores, indicating that the activator melting bridge has not been reached. These results show that $ZnCl_2$ melts and forms bubbles during the cooling phase, which stick to the surface of the biochar, obstructing the pores [37]. Activated biochars P700(p), P700(aq), and P900(p) feature pores that would result from the thermal transformation of $ZnCl_2$, followed by the release of gases (HCl, CO_2, CO, and/or Zn). At temperatures above the melting point, $ZnCl_2$ decomposes and accelerates the volatilization of organic matter, leaving voids or pores [38]. However, in the case of P900(aq), the material begins to degrade and the porous structure gradually collapses. This shows that dry impregnation offers well-developed porosity for P700(p) and P900(p) materials compared to those prepared by wet impregnation, whose pores appear clogged, e.g., P700(aq), or are destroyed (P900(aq)).

3.2. X-Ray Diffraction Characterization

Figure 2 shows the XRD patterns of the BCA(p) and BCA(aq) specimens. Comparison of the two types of biochars provides a better understanding of the effect of activation. Between 2θ (15 and 30°), one can note the presence of peaks and the absence of bumps on all samples, justifying the graphitic or non-amorphous appearance of the biochars. Non-activated biochars (BC) show peaks above $2\theta = 31^\circ$ characteristic of minerals and an intense peak at $2\theta = 31^\circ$ attributed to silica [9]. Following activation with $ZnCl_2$ at 400 °C, the peaks of the minerals Ca, Mg, and Si, which emerged above $2\theta = 40^\circ$ in the P400 case, disappear completely. On the other hand, the silica peak at $2\theta = 31^\circ$ appears only in P400(p), whose intensity has dropped by more than seven times compared with P400. A new peak appears for both activation types at $2\theta = 18.2^\circ$, corresponding to $ZnCl_2$. This is due to the $ZnCl_2$ in solution, which, when converted into Zn^{2+} and Cl^- ions, becomes more reactive and is likely to react with Si. It is as if there were a cationic exchange between the minerals on the biochar surface and the Zn ions, which are eliminated by washing with acid and then distilled water [39].

Figure 2 shows that at 700 °C, the intensity of the characteristic metal peaks decreases, becoming weaker in the case of P700(aq). The $ZnCl_2$ peak disappears for P700(p) and P700(aq) and new peaks appear at 2θ (22.4 and 33.3°) and (29.8 and 36.6°) corresponding to the $Zn_2(SiO_4)$ and ZnO [40,41] peaks, respectively. The presence of the latter stems from the reaction transforming $ZnCl_2$ under the effect of temperature (Equations (7) and (8)):

$$ZnCl_2 + H_2O \rightarrow ZnO + 2HCl\uparrow \quad (7)$$

$$2ZnO + SiO_2 \rightarrow Zn_2(SiO_4) \quad (8)$$

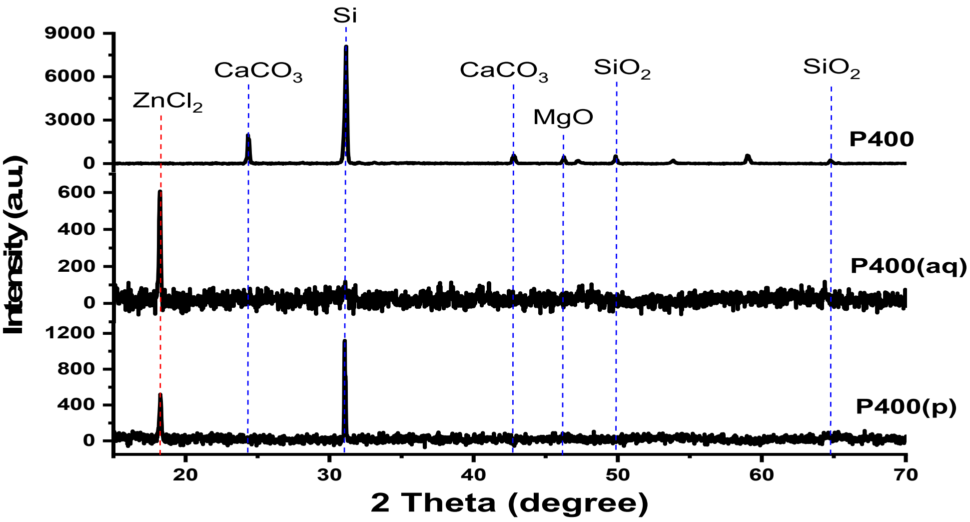

(a)

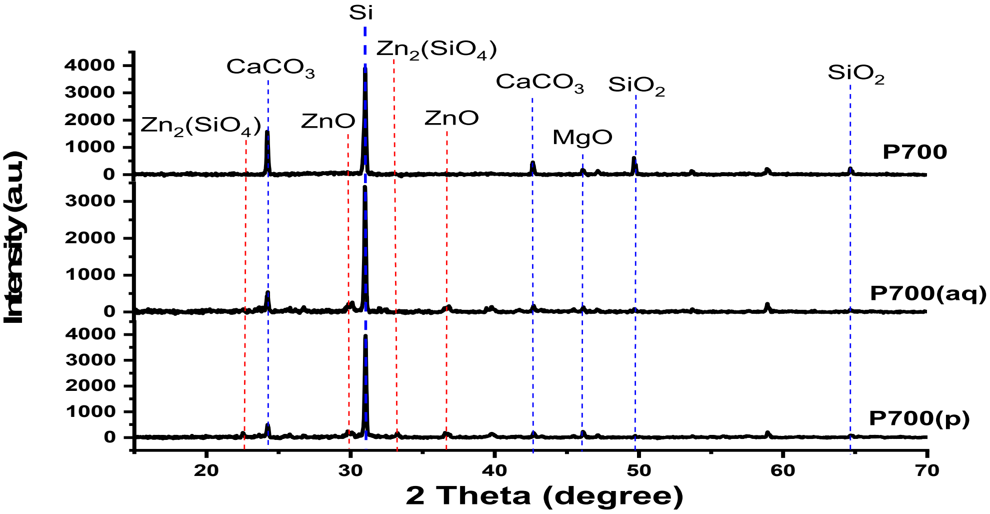

(b)

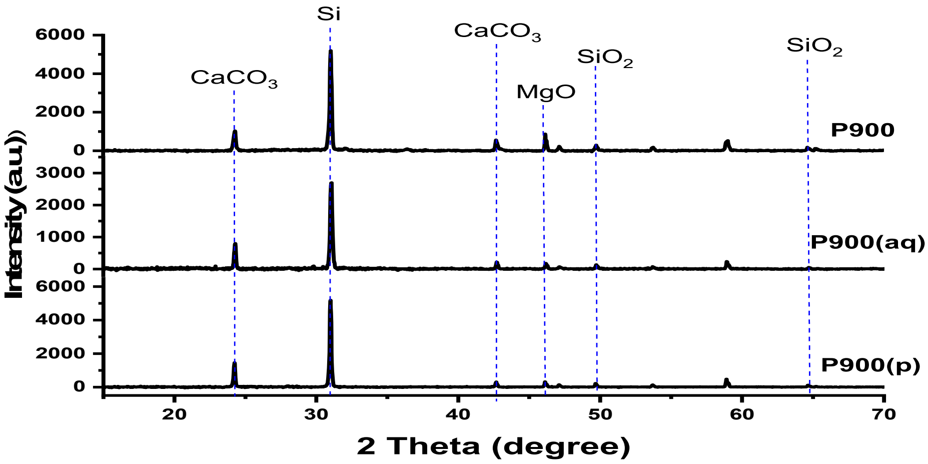

(c)

Figure 2. XRD patterns of the BCA(p), BCA(aq), and BC samples prepared by pyrolysis at 400 (**a**), 700 (**b**), and 900 °C (**c**).

At higher pyrolysis temperatures (900 °C), no characteristic Zn peaks are detected. At this temperature, the reactions continue, ZnO and $Zn_2(SiO_4)$ decompose to produce gas-phase Zn, capable of volatilizing (see Equations (9) and (10)) [42,43]. At 400 °C, P400(aq) and P400(p) exhibit only $ZnCl_2$ as zinc-containing compound, because the pyrolysis temperature is not sufficient to yield ZnO, responsible of carbon oxidation into CO_2 and the formation of pores. For pyrolysis at 700 °C, the only zinc-containing compound probed by XRD is Zn_2SiO_4 which is also known to react with the carbon network to release CO_2 (Equation (10)) thus inducing the formation of pores.

$$2ZnO + C \rightarrow 2Zn \uparrow + CO_2 \uparrow \tag{9}$$

$$Zn_2(SiO_4) + C \rightarrow 2Zn \uparrow + SiO_2 + CO_2 \uparrow \tag{10}$$

3.3. Raman Spectroscopy

Figure S3 shows the Raman spectra recorded in the 800 to 2,000 cm^{-1} energy region. One can note the presence of the bands D* (1380 cm^{-1}), G (1596 cm^{-1}), S (1262 cm^{-1}), V (1506 cm^{-1}), G_L (1696 cm^{-1}), S_L (900 cm^{-1}), characteristic of sp^3 C-X (X = donor atom), graphite sp^2 C=O or sp^2 C=C, sp^3-sp^3 C-C, sp^3 C-Z (Z = heteroatom), sp^2 C=O, and sp^3 C-H, respectively [44]. Figure 3 displays a bar plot of the I_D/I_G intensity ratios for the activated biochars. Lower intensity ratios account for graphitization, while higher values characterize the degree of disorder in the material. P400(aq) is the only material with an I_D/I_G ratio below 1, indicating a particularly ordered BCA. For other materials such as P400(p), P700(aq), P700(p), and P900(aq), P900(p), the I_D/I_G ratio remains above 1, attesting to the disordered nature of these materials [45]. These findings demonstrate that the level of disorganization gives these materials more catalytic sites and a higher adsorption capacity [46].

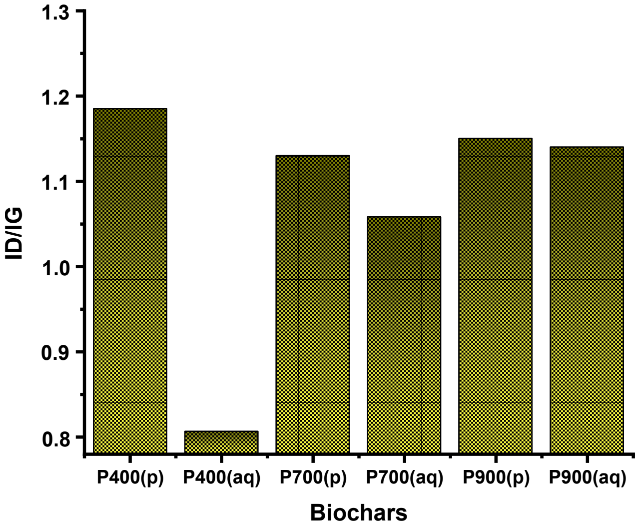

Figure 3. Bar graph of the I_D/I_G intensity ratios determined for BCAs prepared by wet and dry impregnation, at the indicated pyrolysis temperature.

3.4. XPS

Figure 4 displays XPS survey regions (Figure 4a) and the high-resolution C1s spectra (Figure 4b) of the activated biochar samples, at the indicated pyrolysis temperature. The main peaks are Cl2p (~200 eV), C1s (~285 eV), N1s (~400 eV), O1s (~531 eV), and Zn2p (1022–1044 eV). It is worth noting the presence of zinc at the surface of P400(p), despite a thorough acid washing of the biochar, followed by rinsing with copious amounts of water. The presence of zinc, following pyrolysis at 400 °C, is due to an ionic bond between Zn(II) and chlorides, as shown by XRD. Zinc content decreases for a higher pyrolysis temperature, i.e., 700 °C, and particularly 900 °C (Figure 4a). Pyrolysis at 900 °C of the dry impregnated biomass facilitates the release of zinc; its boiling temperature is 907 °C. The Zn/C atomic ratio decreases sharply with pyrolysis temperature (inset of Figure 4a). We have determined α' the modified Auger parameter and found it to be equal to 2009.9–2010.2 eV, which is in line with zinc in the oxidized state. Indeed, α' = 2013.8 eV for zinc in the metallic state [47]. The C1s regions show a decrease in the full width at half maximum (FWHM) at high pyrolysis temperature, from 1.7 eV to 1.45 ± 0.05 eV. The higher FWHM obtained for P400(p) is due to the contribution of C-N, C-O and O-C=O chemical environments to the C1s peak. For example, the C/(O + N) atomic ratio increases with pyrolysis; *i.e.*, it is equal to 2.6, 9.6, and 6.9 for P(400)p, P(700)p, and P(900)p, respectively. It follows that one obtains a carbon-richer material with narrower C1s peak.

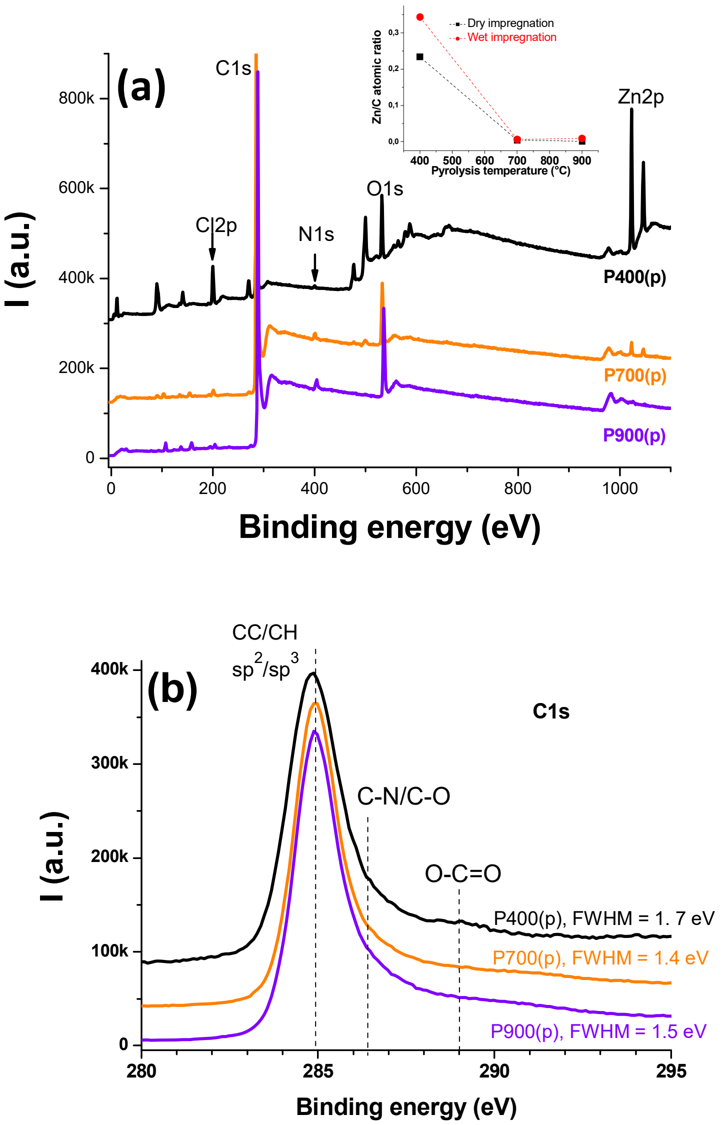

Figure 4. Survey regions (**a**) and high-resolution C1s spectra (**b**) of activated biochars prepared by pyrolysis at 400, 700, and 900 °C. Zn/C atomic ratio vs. temperature is shown in the inset.

Figure 5a,c,e shows high resolution N1s spectra, fitted with either 3 or 4 components. P400(p) N1s (Figure 5a) has pyridinic (~398.5 eV), pyrrolic (~400 eV), and graphitic (401–402 eV) nitrogen atoms. The peak component at 401–402 eV, could also be partially due to pyridinic oxide [48,49]. It is worth noting the significant change in the shape of the N1s region, with a higher relative intensity of the pyridinic nitrogen atom component (Figure 5c,e), compared to the N1s peak component ascribed to pyrrolic nitrogen atoms. A fourth component can also be noted, and due to N-O (~405 eV) [50] in alkyl nitrite chemical environment [51], for activated biochar prepared at 700 or 900 °C (Figure 5c,e).

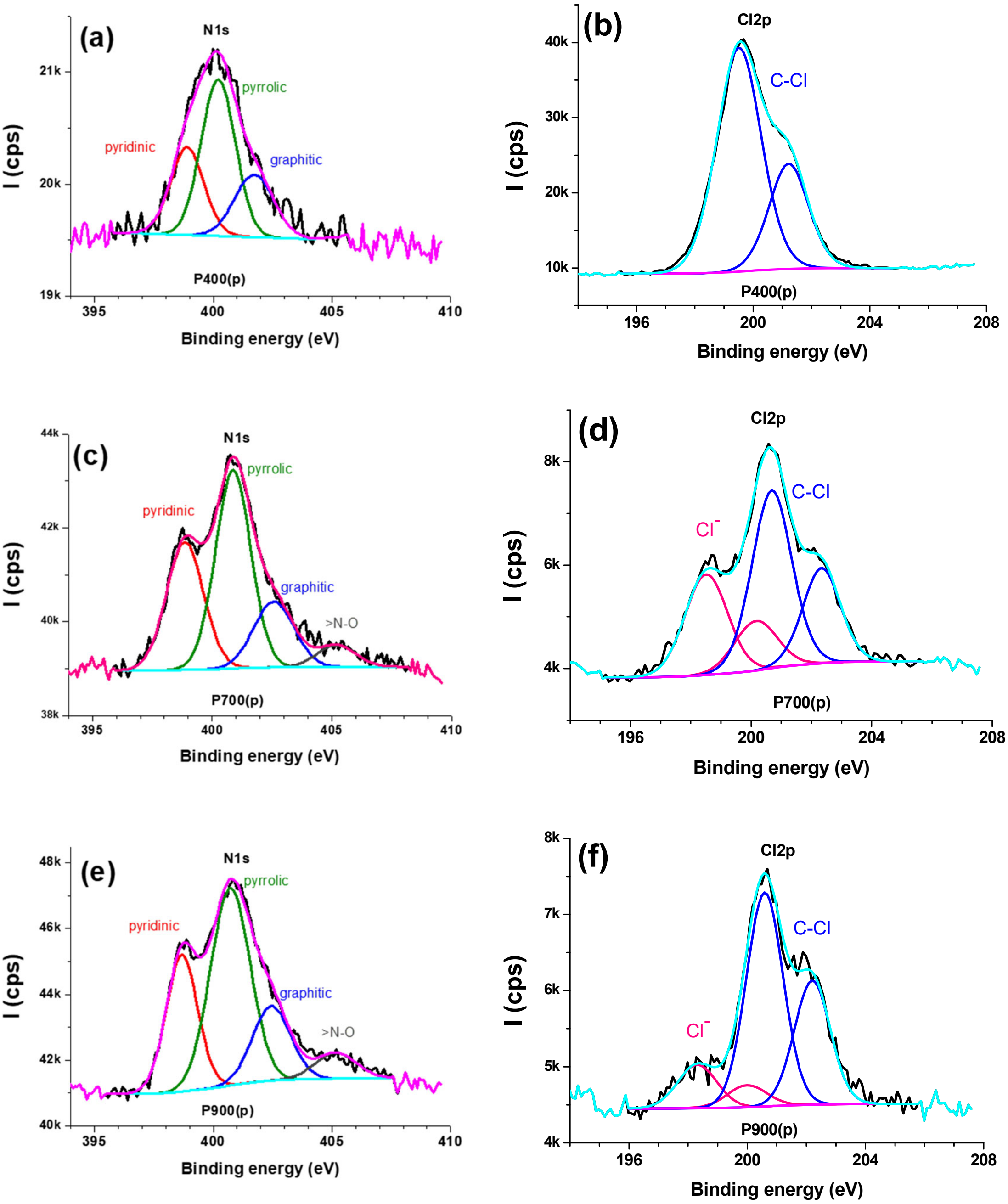

Figure 5. High-resolution, peak-fitted N1s and Cl2p spectra of (**a**,**b**) P400(p), (**c**,**d**) P700(p), and (**e**,**f**) P900(p).

Cl2p spectrum is a doublet, of which components are split by 1.6–1.7 eV, with an intensity ratio $Cl2p_{3/2}/Cl2p_{1/2} = 2$. The doublet peak position is in line with the C-Cl bond for the biochar prepared at 400 °C (Figure 5b). For pyrolysis conducted at 700 and 900 °C, a second doublet is noted and assigned to chlorides (Figure 5d,f). The presence of Cl^- could be due to remaining $ZnCl_2$, C-Cl bond cleavage, and retention of the chlorides, despite thorough rinsing with water. Apart from that, it is possible that NH_4Cl forms during the initial stages of carbonization. This inorganic compound decomposes at 338 °C under N_2, with the release of NH_3 and HCl [52]. However, HCl likely reacts with some nitrogen sites from the forming biochar to obtain:

$$N- + HCl \longrightarrow \equiv N^{+}HCl^{-}. \tag{11}$$

Another possible reason for the presence of chlorides is the reaction of biochar-Cl with ZnO at moderate temperature, which induces the reduction of Zn(II) into zero valent zinc, hence the appearance of chlorides [53]. The concomitant presence of Cl^{-} and N-O bonds on the biochar surface for high pyrolysis temperature is likely to be related to the disorder in the biochar structure, observed in the Raman spectra of P700(p) and P900(p).

3.5. Determination of MB and Iodine Indices

Figure 6 displays the bar graphs of N_{MB} and N_I values for the various active biochars. For dry impregnation, Figure 6a shows that the N_I of BCA(p) increases from P400(p) to P700(p), with N_I values of 274 and 664 mg.g^{-1}, respectively, then decreases to 473.3 mg.g^{-1} for P900(p). For BCA(aq), there is a gradual increase in N_I value as a function of pyrolysis temperature. The results show that P700(p) has the highest N_I value, demonstrating that microporosity is affected by both temperature and activation type. As shown in Figure 6b, N_{MB} values increase with pyrolysis temperature, reaching near their maximum at 700 °C for the BCA(p) and BCA(aq) cases. For P400(p) and P400(aq), N_{MB} values remain low, i.e., below 40 mg g^{-1}. This trend suggests that mesoporosity depends on temperature and volatile substance concentration. It is worth noting that NI and NMB correlate well with the micropore and mesopore volumes determined by nitrogen adsorption isotherms [29], and could thus be regarded as a simple and cost-effective approach to study biochar pore volume. Moreover, Table S1 shows that biochars produced by dry impregnation at 700 °C and 900 °C exhibit significantly larger active surface areas, with sample P700(p) showing the highest value. In contrast, the low-temperature samples (P400(aq) and P400(p)) possess the smallest surface areas. This trend is consistent with the iodine index results, confirming that the active surface area of biochars is closely related to the development of surface microporosity.

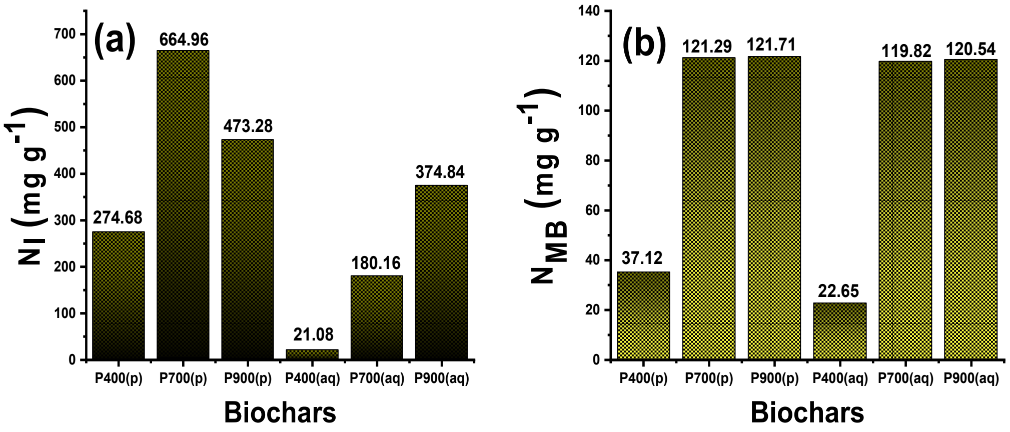

Figure 6. Iodine number (**a**), and methylene blue number (**b**) of BCAs.

3.6. Electrochemical Characterization

Figure 7 illustrates the study of the electrochemical properties of the surface of GC electrodes modified with different BCA materials, such as P400(p), P400(aq), P700(p), P700(aq), P900(p), and P900(aq) was carried out by cyclic voltammetry and impedance spectroscopy. The inset in Figure 7a shows a zoomed-in view of the voltammograms for the bare electrode and the electrode materials P400(p) and P400(aq). These cyclic voltamograms all display the same quasi-rectangular symmetrical arrangement with no oxidation or reduction points (peaks). This suggests an EDC energy storage behavior of these composite biochar materials [54], which is well in line with porous carbon-based materials [55]. Furthermore, a comparative study of the CV profile of the different biochar materials P400(aq), P400(p), P700(p), P700(aq), P900(p), and P900(aq) reveals a significantly higher overall surface area for P700(p), indicating that this material has better electroactivity. In other words, pyrolysis at 700 °C gives biochars superior conductivity compared to others, attesting to their outstanding performance and ideal capacitance characteristics. Electrochemical impedance spectroscopy (EIS) measurements were also carried out for BCA coatings deposited on GC to assess the interracial properties of GC electrodes, specifically P400(aq), P400(p), P700(aq), P700(p), P900(aq), and P900(p). Figure 7b shows the Nyquist curves obtained at open circuit potential in 0.5 M H_2SO_4. The inset in 7b corresponds to the zoom-in Nyquist plots for P700(p), P700(aq), P900(p), and P900(aq). As observed, the Nyquist curves consist of a semicircle appearing in the high-frequency region and a slope in the low-frequency region, reflecting ideal supercapacitive behavior [56]. A study of the electron transfer capacity of the various electrodes showed that the presence of BCA on the surface of the GC electrode induces a significant decrease in charge transfer resistance (Rct), clearly indicating that the millet bran biochar is sufficiently conductive. Rct values decrease in the following order: GCE (168 Ω) > P400(aq) (144 Ω) > P400(p) (50.3 Ω) > P700(aq) (40.4 Ω) > P900(aq) (19.1 Ω) > P900(p) (18.3 Ω) > P700(p) (2.5 Ω). The lower charge transfer resistance value of the P700(p) electrode material indicates an easier electron transfer process, obtained for dry impregnation and pyrolysis at 700 °C. These results suggest that the obstructive effect of pores leads to a reduction in the rate of electron transfer or an increase in resistance to electron flow [23].

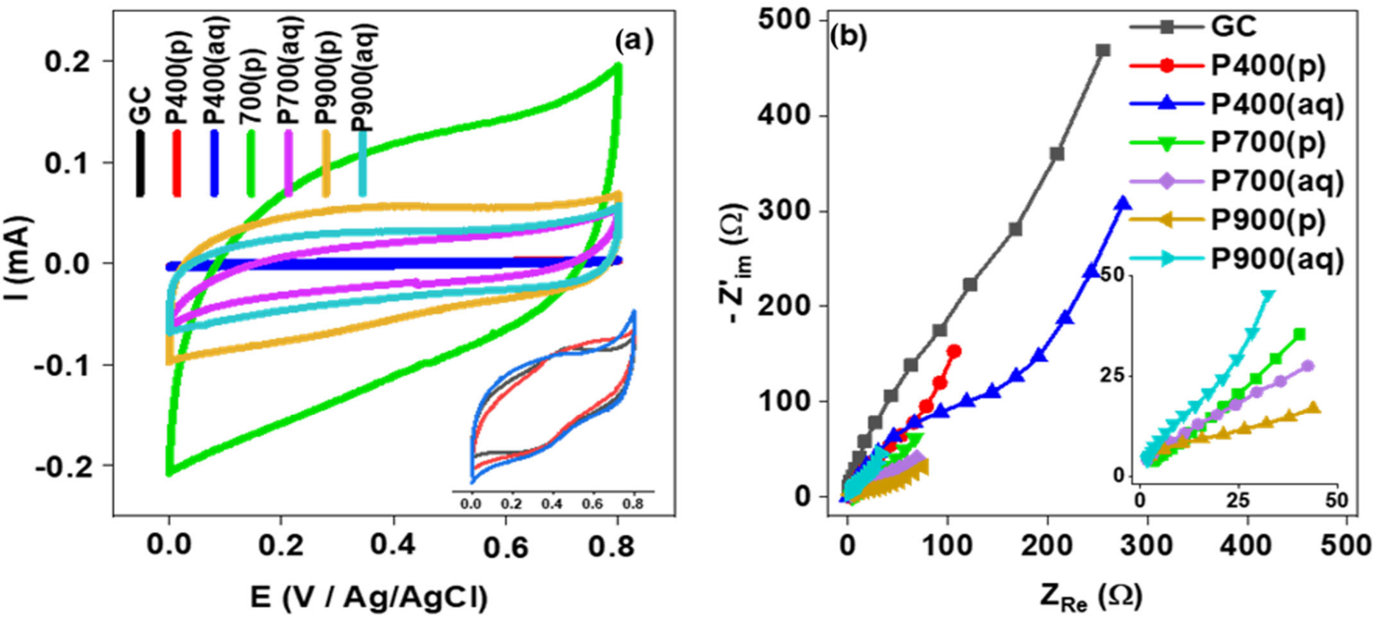

Figure 7. (**a**) CV curves recorded at a scan rate of 50 mV s^{-1}. In the insert, the zoom of GC, P400(p), P400(aq); and (**b**) EIS plots recorded for GC and activated biochar electrode materials. In insert the zoom of P700(p), P700(aq), P900(p), and P900(aq).

Next, we attempted to correlate the specific capacitance (determined from the CV plots, see Equation (3)), with porous volume descriptors N_I and N_{MB}. Figure 8a shows that P700(p) has a significantly higher specific capacitance and N_I value than the other materials. Moreover, P400(p) has a higher N_I value than P700(aq) while exhibiting a lower Csp value, suggesting that specific capacitance is not solely dependent on microporosity. Additionally,

Figure 8b shows that materials P700(p), P700(aq), P900(p), and P900(aq) exhibit similar N_{MB} values despite their differing Csp values, suggesting that mesoporosity has a minimal influence on the specific capacitance.

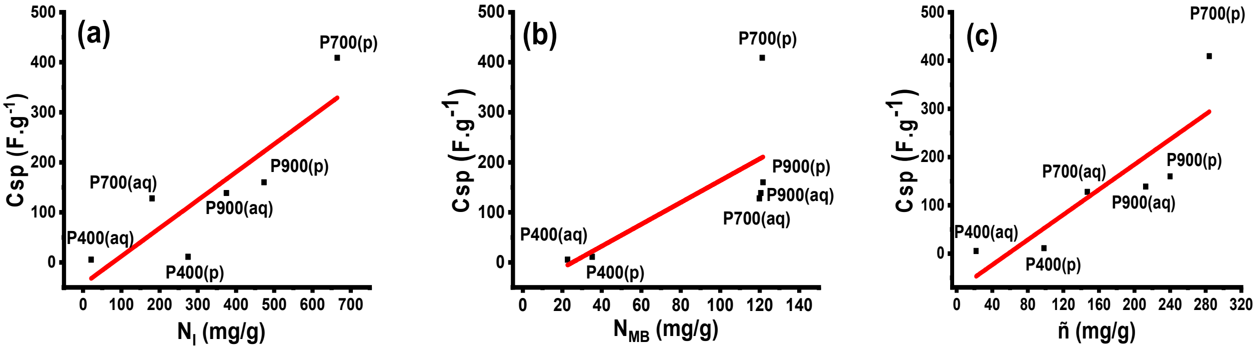

Figure 8. Plots of specific capacitance (Csp) versus (**a**) iodine number, (**b**) methylene blue number, and (**c**) the geometric mean value of N_{MB} and N_I.

To gain further insight into the relationship between porosity and Csp, we investigated how ñ changes with Csp (Figure 8c). This graph demonstrates a gradual increase in Csp with increasing ñ, indicating that the Csp value correlates with the geometric mean. These findings show that, considered together, micropores and mesopores influence Csp and contribute to high ionic mobility in supercapacitor materials. They also align with research on various biochars, which demonstrates that a higher volume of micropores and mesopores enhances the electrode's specific capacity [57,58]. For example, Csp was found to correlate well with the total pore or mesopore volume of KOH-activated corn straw biochar [57]. The combination of micropores and mesopores in a material represents a significant advantage. Electrochemical and spectroscopic characterizations indicate that the P700(p) material exhibits optimal properties. Therefore, it will be selected as the electrode material for subsequent studies of the supercapacitive behavior of BCAs under galvanostatic conditions.

3.7. Supercapacitor Studies

The supercapacitive behavior of the P700(p) electrode material was assessed in a 0.5 M H_2SO_4 electrolyte solution using the three-electrode setup described above. The CV and Csp curves, as a function of sweep rate variation (10 to 100 mV s^{-1}), are shown in Figure 9 (a and b, respectively). The area of the cyclic voltammograms increases with the scan rate without any distortion, indicating efficient ion transport and excellent capacitive behavior of the P700(p) material [59]. Additionally, the shape of the voltammograms suggests the presence of an EDLC. Regarding Csp, it decreases with the scan rate, from 673 F g^{-1} at 10 mV s^{-1} to 341 F g^{-1} at 100 mV s^{-1}. This trend arises because lower scan rates give ions in the electrolyte less kinetic energy, providing more time for migration and diffusion into the BCA micropores [60]. The GCD curves obtained at different current densities ranging from 0.5 to 5 A g^{-1} (Figure 9c) show a decrease in charge/discharge times as the applied current increases. Both low sweep rates and low current densities promote maximum charge storage across the active sites. Unlike the cyclic voltammograms, the GCD curves do not show perfect potential-time linearity, likely due to the internal resistance of the material or difficulty in accessing small pores [46].

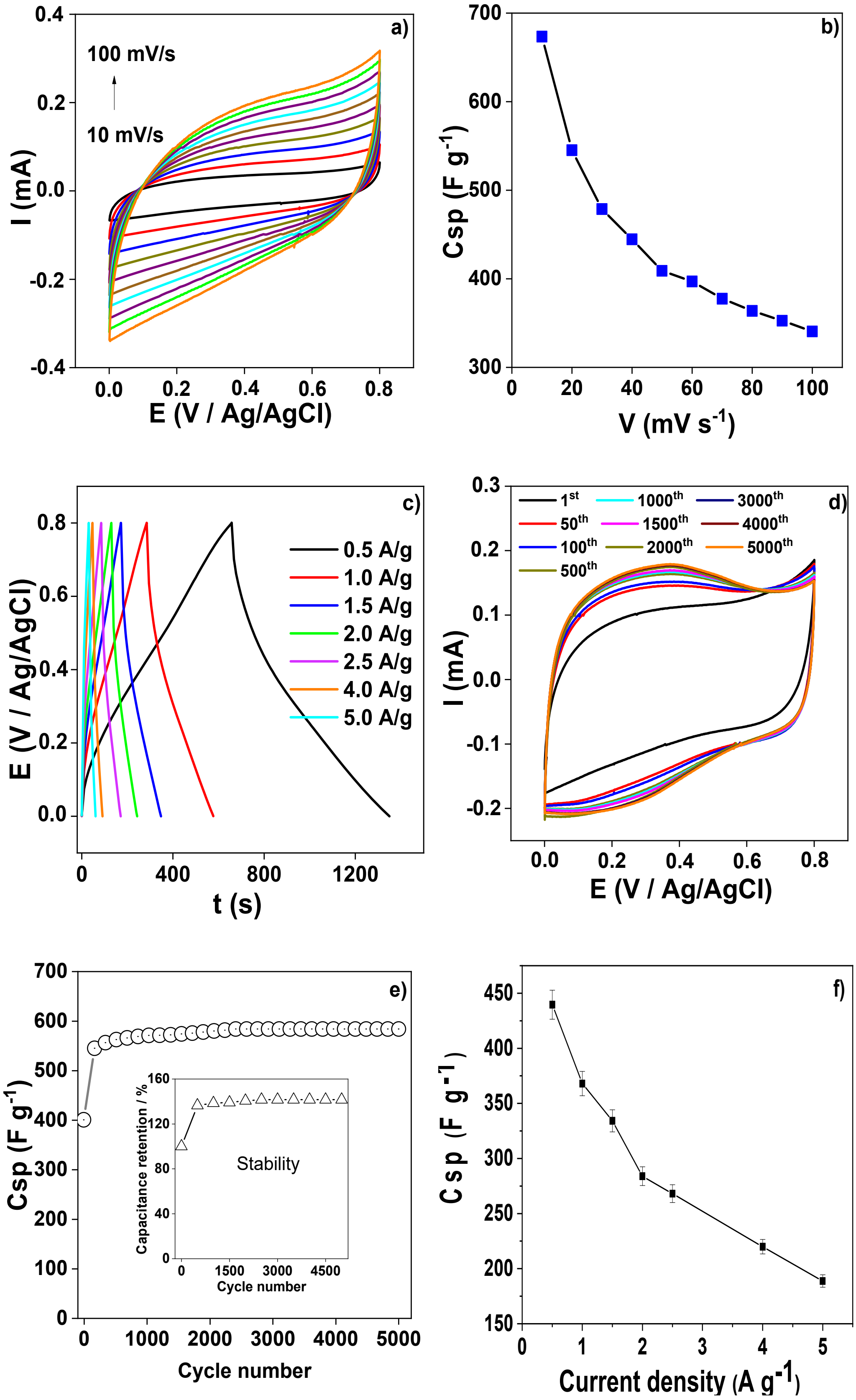

Figure 9. (**a**) CV and (**b**) Csp curves versus scan rate variation (10 to 100 mV/s), (**c**) GCD curves at different current densities, (**d**) CV and (**e**) Csp and capacitance retention curves versus cycle number, and (**f**) specific capacitance versus the current density plot.

From GCD measurements (Figure 9c), a specific capacitance of 440 F g^{-1} was obtained at a current density of 0.5 A g^{-1}, and ~175 F g^{-1} for a current density of 5 A g^{-1} (Figure 9f). The cyclic stability test, which assesses the electrochemical stability of electrode materials over multiple cycles, was performed on BCA P700(p) at a scan rate of 50 mV s^{-1} for 5000 cycles. The CV, Csp, and capacitance retention curves as a function of cycle number are shown in Figure 9d,e. It is evident that this new millet bran-based biochar material exhibits good stability, with a capacitance retention of ~130%, after 5000 cycles. The significant increase in capacitance retention is likely caused by continuous electrochemical activation [61] of inaccessible catalytic sites, thereby improving electron transfer at the electrode/electrolyte interface. In other words, certain sites become activated as the number of cycles increases, which in turn boosts the capacitance retention during cycling [23,62]. These results show a remarkable capacitance retention for the P700(p) electrode material and are in line with other studies. Zhu et al. [62] reported an increase of capacitance retention as high as 242.9% after 10,000 cycles for N-doped Cu_7S_4/carbon felt, whereas Wang et al. [63] reported a capacitance retention of 120% after 5000 cycles for CO_3O_4@MnO_2@PPy/activated carbon. The group of Maboudian [61] reported an increase of 150% in the capacitance retention for unactivated carbon, in H_2SO_4, which is in line with the results discussed in this work. A polyaniline/carbon composite was found to be highly stable with a capacitance retention of 225% after 10,000 cycles [64]. Figure 9f displays a plot of specific capacitance versus the current density.

Table 1 illustrates the specific capacitance values of various electrode materials cited in the literature, developed from metal oxide and biochar. P700(p) exhibits a Csp that exceeds those of modified metal oxides and some biochars. However, it has lower capacity values than BC@MnO_2 which is based on MnO_2, a well-known supercapacitor, whereas SGB has a higher specific capacitance but the capacitance retention levels off at 107% after 12,000 cycles. Nevertheless, the millet bran-derived biochar is an excellent energy storage material that meets the requirements of green, renewable energy. For P700(p), an energy density (E) of 39.1 Wh kg^{-1} and a power (P) of 0.20 kW kg^{-1} were determined. This material demonstrates excellent electrochemical properties, meeting the requirements for supercapacitors and batteries, which are often limited by their energy density values, typically below 20.0 Wh kg^{-1} [65]. Interestingly, it is obtained at moderate pyrolysis temperature and without the use of an excessive initial $ZnCl_2$/biomass ratio.

Table 1. Comparison of Csp values of P700(p) and those of related materials.

Electrode Materiels	**Electrolyte**	**Current Density (A g^{-1})**	**Csp (F g^{-1})**	**Ref**
Fe_2O_3/GA	0.5 M Na_2SO_4	1	81.3	[66]
NCA	1 M H_2SO_4	0.1	NCA-800: 166 NCA-900: 136	[67]
HC2	2 M KOH	0.5	80	[68]
Biochar litchi seed	1 M H_2SO_4	1	190	[69]
Biochar apricot shell	3 M KOH	0.5	216	[70]
BC@MnO_2	1 M Na_2SO_4	0.5	512	[71]
SGB-700	1 M H_2SO_4	0.5	638	[72]
RSBC	6 M KOH	0.2	RSBC: 197.2 RSBC-2: 296	[73]
P700(p)	0.5 M H_2SO_4	0.5	440	This work

Fe_2O_3/GA: nano-iron oxide (Fe_2O_3)/three-dimensional graphene aerogel. NCA: nitrogen-doped carbon aerogels. HC2: nitrogen-doped hydrochar from sawdust biomass activated with KOH. Biochar litchi seed: Litchi seed-derived biochar. Biochar apricot shell: apricot shell-derived biochar activated by KOH. BC@MnO_2: Acacia leucopheloea wood sawdust (ALWSD) biochar-supported MnO_2 nanocomposite. SGB-700: Suaeda Glauca Bunge (SGB) derived biochar. RSBC: rice straw biochar activated at 800 °C. RSBC-2: rice straw biochar activated at 800 °C with KOH.

The pending question is whether the amount of zinc leftover in P700(p), despite thorough washing, contributes to the specific capacitance. Indeed, Madhu et al. [74] demonstrated that the specific capacitance of sugarcane bagasse activated carbon increases from 92 to 127 F g^{-1} upon addition of 10 wt.% ZnO. Furthermore, research by Kandhasamy et al. shows that $Zn_2(SiO_4)$ increases the specific capacitance of the material from 164.4 to 227.5 F·g^{-1} [75]. Returning to this work, an unwashed P700(p) sample was characterized by XPS, XRD, and electrochemistry (Figure 10). Figure 10a compares the survey regions of the washed and unwashed P700(p) samples. The washing with HCl, followed by water, yields a drastic decrease in the content of zinc, and therefore the Zn/C (x1000) atomic ratio, from 14 to 4.02. This is confirmed by XRD (Figure 10b), which accounts for the removal of several species from the biochar upon washing (note the significant decrease in the peak intensity of the ZnO peaks). Finally, electrochemical testing shows enhanced electroactivity of the washed sample as depicted by the CV plots in Figure 10c. The GCD plots displayed in Figure 10d show a slower discharge of the washed P700(p) sample. Clearly, the ZnO does not improve the specific capacitance of the biochar under test. A close inspection of the XRD patterns undoubtedly shows the removal of ZnO peaks upon washing. The small portion of Zn_2SiO_4 retained in the biochar could improve the Csp, which is in line with the literature [75].

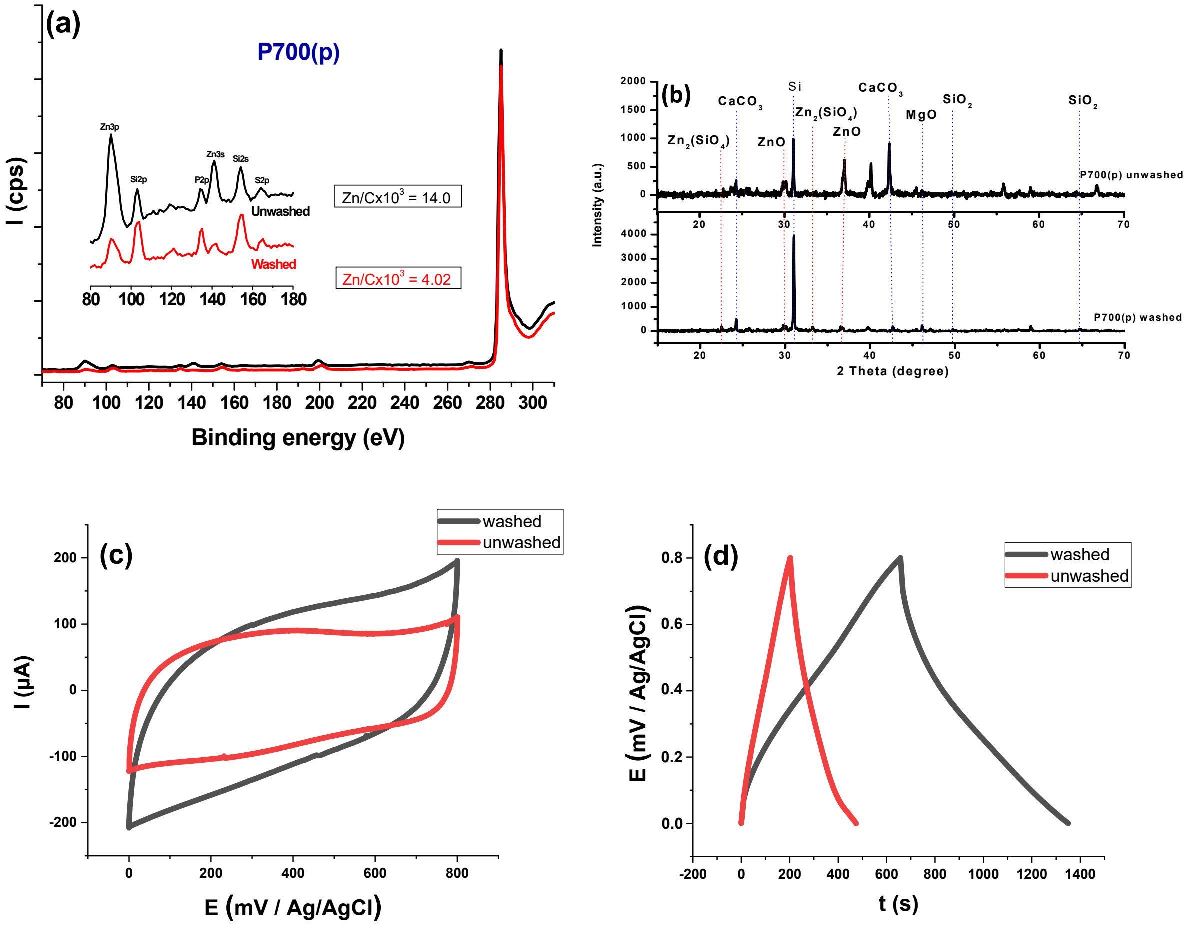

Figure 10. XPS survey regions (**a**), XRD patterns (**b**), cyclic voltammograms (**c**), and GCD plots (**d**) for the washed and unwashed P700(p) samples.

For a practical demonstration, the specific capacitance was determined for a two-electrode configuration. Figure 11 shows the CV and GCD plots for P700(p). Whilst the CV shape is similar to that displayed in Figure 9c, the GCD shows a faster discharge. The Csp in a two-electrode configuration was calculated using:

$$C_{Sp} = \frac{I}{m \times \left(\frac{dV}{dt}\right)} \tag{12}$$

where *I(A):* discharge current; dV/dt: slope of discharge curve, and m: total mass of the active materials of the two electrodes [76]. It was to equal 110 F g^{-1}, lower than that reported for the three-electrode configuration, in agreement with the literature [77,78].

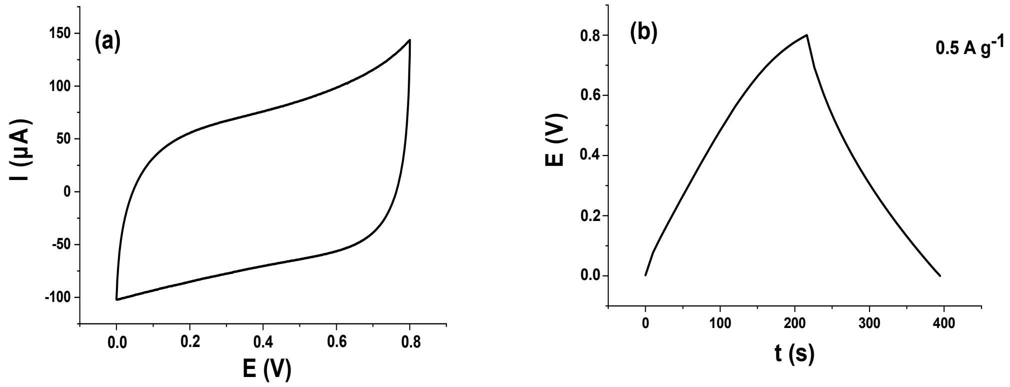

Figure 11. CV (**a**) and GCD (**b**) plots for P700(p) in two-electrode configuration.

4. Conclusions

Activated biochars were prepared by impregnation of millet bran biomass with $ZnCl_2$ powder or $ZnCl_2$ solution (dry and wet impregnation). Both the temperature and the way the biomass was activated affected the electrochemical performance of the biochars. Porosity was monitored via iodine and methylene blue indices. XPS analysis showed the absence of zinc at high pyrolysis temperature, and suggested complex reaction between $ZnCl_2$ and the biochar leading to C-Cl bonds, and also tightly bound zinc at low pyrolysis temperature, despite post acid wash of the biochar. These observations were corroborated by XRD, which confirmed the absence of zinc-specific peaks after acid washing, particularly in the case of P700(p). SEM pictures of BCAs revealed well elaborated pores, helping to increase electron transport and improve material conductivity. Electrochemical analyses have demonstrated the superior energy storage performance of an EDLC supercapacitor at optimum efficiency. The P700(p) material had the highest N_I value, a significant N_{MB} value, and a specific capacitance of 440 F g^{-1} at 0.5 A g^{-1}, with an energy density of 39.1 W h kg^{-1}. Moreover, the capacitive retention is 130% after 5000 cycles, possibly due to electrochemical activation during the charge-discharge process. In the two-electrode configuration, the Csp was found to equal 110 F g^{-1}, lower than in the three-electrode configuration. It was further demonstrated that unwashed activated biochar retained more ZnO, but this compound did not enhance the specific capacitance. The high specific capacitance is primarily dependent of the porous structure, and at a lesser extent the small amounts of Zn_2SiO_4, retained in the biochar, despite thorough washing.

This work demonstrates that the $ZnCl_2$ activating agent used in the dry impregnation method confers exceptional electrochemical performance on the materials. These results highlight the opportunity to exploit materials derived from bio-waste for energy storage systems, which not only helps to address environmental issues but also optimizes the economic and performance metrics of supercapacitors, thus contributing to addressing UNs' SDG7 relevant to Affordable and Clean Energy.

Supplementary Materials: The following supporting information can be downloaded at: https://www.mdpi.com/article/10.3390/surfaces8040087/s1, Figure S1: CV plots at indicated potential windows, for P700(p). Scan rate=50 mV s^{-1}. Table S1. Active surface area of biochar samples used as working electrodes. Figure S2: SEM images of biochar samples prepared by wet (aq) and dry (p) impregnation with $ZnCl_2$, at 400, 700 and 900 °C. Figure S3: Raman spectroscopy of (a) P400(p), (b) P400(aq), (c) P700(p), (d) P700(aq), (e) P900(p), and (f) P900(aq).

Author Contributions: C.A.B.D.: Writing—review & editing, Writing—original draft, Validation, Conceptualization, Data Curation. D.F.: Writing—review & editing, Writing—original draft, Validation; M.L.: Writing—review & editing, Writing—original draft, Validation, Conceptualization; D.B.: Investigation, Formal analysis, Writing-review & editing; H.W.: Visualization, Validation, Investigation; M.E.G., Investigation, Data Curation, Writing—review & editing; V.S.: Investigation, Data Curation, Writing—review & editing; A.M.: Investigation, Validation, Writing—review & editing; M.J.: Investigation, Validation, Writing—review & editing; D.G.-S.: Funding, Conceptualization, Writing—review & editing; M.M.C.: Conceptualization, Data curation, Validation, Writing—review & editing, Supervision. All authors have read and agreed to the published version of the manuscript.

Funding: The authors are indebted to the Senegalese Ministry of Higher Education, Research and Innovation (MESRI) for the provision of a fellowship to C.A.B. Diop.

Data Availability Statement: Data will be made available on request.

Conflicts of Interest: The authors declare that they have no known competing financial interests or personal relationships that could have appeared to influence the work reported in this paper.

References

1. Jellali, S.; Dutournié, P.; Jeguirim, M. Materials and clean processes for sustainable energy and environmental applications: Foreword. *Comptes Rendus Chim.* **2023**, *26*, 3–5. [CrossRef]
2. Kebede, A.A.; Kalogiannis, T.; Van Mierlo, J.; Berecibar, M. A comprehensive review of stationary energy storage devices for large scale renewable energy sources grid integration. *Renew. Sustain. Energy Rev.* **2022**, *159*, 112213. [CrossRef]
3. Şahin, M.E.; Blaabjerg, F.; Sangwongwanich, A. A Comprehensive Review on Supercapacitor Applications and Developments. *Energies* **2022**, *15*, 674. [CrossRef]
4. Sharma, S.; Chand, P. Supercapacitor and electrochemical techniques: A brief review. *Results Chem.* **2023**, *5*, 100885. [CrossRef]
5. Dar, M.A.; Majid, S.; Satgunam, M.; Siva, C.; Ansari, S.; Arularasan, P.; Ahamed, S.R. Advancements in Supercapacitor electrodes and perspectives for future energy storage technologies. *Int. J. Hydrogen Energy* **2024**, *70*, 10–28. [CrossRef]
6. Zhai, Z.; Zhang, L.; Du, T.; Ren, B.; Xu, Y.; Wang, S.; Miao, J.; Liu, Z. A review of carbon materials for supercapacitors. *Mater. Des.* **2022**, *221*, 111017. [CrossRef]
7. Chen, W.; Shi, X.; Peng, Y.; Wang, Y.; Li, J.; Wang, Y.; Gong, C.; Dong, C.; Gao, S.; Xu, L.; et al. Biomass pyrolysis for N-doped biochar: Relationship among preparation process, N-doped biochar properties, and supercapacitors. *Fuel* **2025**, *404*, 136372. [CrossRef]
8. Mahmood, F.; Ali, M.; Khan, M.; Mbeugang, C.F.M.; Isa, Y.M.; Kozlov, A.; Penzik, M.; Xie, X.; Yang, H.; Zhang, S.; et al. A review of biochar production and its employment in synthesizing carbon-based materials for supercapacitors. *Ind. Crop. Prod.* **2025**, *227*, 120830. [CrossRef]
9. Diop, C.A.B.; Lo, M.; Snoussi, Y.; Gam-Derouich, S.; El Garah, M.; Jouini, M.; Gningue-Sall, D.; Chehimi, M.M. Functional hydrochar/biochar through thermochemical conversion of millet Bran from Senegal: Physicochemical, morphological and electrochemical properties. *Emergent Mater.* **2025**, *8*, 2663–2678. [CrossRef]
10. Ahmad, M.; Rajapaksha, A.U.; Lim, J.E.; Zhang, M.; Bolan, N.; Mohan, D.; Vithanage, M.; Lee, S.S.; Ok, Y.S. Biochar as a sorbent for contaminant management in soil and water: A review. *Chemosphere* **2014**, *99*, 19–33. [CrossRef]
11. Wang, D.; Li, C.; Parikh, S.J.; Scow, K.M. Impact of biochar on water retention of two agricultural soils—A multi-scale analysis. *Geoderma* **2019**, *340*, 185–191. [CrossRef]
12. Kumar, A.; Sharma, K.; Dixit, A.R. Carbon nanotube- and graphene-reinforced multiphase polymeric composites: Review on their properties and applications. *J. Mater. Sci.* **2019**, *55*, 2682–2724. [CrossRef]
13. Bassyouni, M.; Mansi, A.E.; Elgabry, A.; Ibrahim, B.A.; Kassem, O.A.; Alhebeshy, R. Utilization of carbon nanotubes in removal of heavy metals from wastewater: A review of the CNTs' potential and current challenges. *Appl. Phys. A* **2019**, *126*, 38. [CrossRef]
14. Li, X.; Zhang, J.; Liu, B.; Su, Z. A critical review on the application and recent developments of post-modified biochar in supercapacitors. *J. Clean. Prod.* **2021**, *310*, 127428. [CrossRef]

15. Uppugalla, S.; Pothu, R.; Boddula, R.; Desai, M.A.; Al-Qahtani, N. Nitrogen and sulfur co-doped activated carbon nanosheets for high-performance coin cell supercapacitor device with outstanding cycle stability. *Emergent Mater.* **2023**, *6*, 1167–1176. [CrossRef]
16. Sandeep, A.; Ravindra, A.V. Peanut shell-derived porous carbons activated with iron and zinc chlorides as electrode materials with improved electrochemical performance for supercapacitors. *Emergent Mater.* **2024**, *8*, 235–250. [CrossRef]
17. Gęca, M.; Khalil, A.M.; Tang, M.; Bhakta, A.K.; Snoussi, Y.; Nowicki, P.; Wiśniewska, M.; Chehimi, M.M. Surface Treatment of Biochar—Methods, Surface Analysis and Potential Applications: A Comprehensive Review. *Surfaces* **2023**, *6*, 179–213. [CrossRef]
18. Hagemann, N.; Spokas, K.; Schmidt, H.-P.; Kägi, R.; Böhler, M.A.; Bucheli, T.D. Activated Carbon, Biochar and Charcoal: Linkages and Synergies across Pyrogenic Carbon's ABCs. *Water* **2018**, *10*, 182. [CrossRef]
19. Velusamy, K.; Isabel, J.B.; Periyasamy, S.; Thiruvenkadam, A.; Ravikumar, H.; Gupta, S.K.; López-Maldonado, E.A. Role of biochar as a greener catalyst in biofuel production: Production, activation, and potential utilization—A review. *J. Taiwan Inst. Chem. Eng.* **2024**, *177*, 105732. [CrossRef]
20. Yuan, X.; Cao, Y.; Li, J.; Patel, A.K.; Dong, C.-D.; Jin, X.; Gu, C.; Yip, A.C.; Tsang, D.C.; Ok, Y.S. Recent advancements and challenges in emerging applications of biochar-based catalysts. *Biotechnol. Adv.* **2023**, *67*, 108181. [CrossRef]
21. Zhou, X.; Zhu, Y.; Niu, Q.; Zeng, G.; Lai, C.; Liu, S.; Huang, D.; Qin, L.; Liu, X.; Li, B.; et al. New notion of biochar: A review on the mechanism of biochar applications in advanced oxidation processes. *Chem. Eng. J.* **2021**, *416*, 129027. [CrossRef]
22. Abdu, H.I.; Mahmood, S.A.; Aboudou, T.; Guo, Y.; Nian, L.N.; Xiaowei, L.; Ziyu, L.; Jlassi, K.; El-Demellawi, J.K.; Eid, K. Hierarchical porous carbon biochar nanotubes encapsulated metal nanocrystals with a strong metal-carbon interaction for high-performance supercapacitors. *Ultrason. Sonochem.* **2025**, *121*, 107476. [CrossRef] [PubMed]
23. Lima, R.M.A.P.; dos Reis, G.S.; Thyrel, M.; Alcaraz-Espinoza, J.J.; Larsson, S.H.; de Oliveira, H.P. Facile Synthesis of Sustainable Biomass-Derived Porous Biochars as Promising Electrode Materials for High-Performance Supercapacitor Applications. *Nanomaterials* **2022**, *12*, 866. [CrossRef] [PubMed]
24. Zhang, K.; Sun, J.; E, L.; Ma, C.; Luo, S.; Wu, Z.; Li, W.; Liu, S. Effects of the Pore Structure of Commercial Activated Carbon on the Electrochemical Performance of Supercapacitors. *J. Energy Storage* **2022**, *45*, 103457. [CrossRef]
25. Wang, L.; Bai, R.; Tian, Y.; Yang, C.; Tian, X. ZnCl2 activation tailoring microporous architecture in wheat straw-derived biochar for enhanced sulfamethoxazole adsorption. *J. Water Process. Eng.* **2025**, *77*, 108617. [CrossRef]
26. Nunes, C.A.; Guerreiro, M.C. Estimation of surface area and pore volume of activated carbons by methylene blue and iodine numbers. *Quimica Nova* **2011**, *34*, 472–476. [CrossRef]
27. Chetima, A.; Bup, D.N.; Kewir, F.; Wahaboua, A. Activated carbons from open air and microwave-assisted impregnation of cotton and neem husks efficiently decolorize neutral cotton oil. *Heliyon* **2024**, *10*, e24060. [CrossRef]
28. Mishra, P.K.; Aryal, S.; Oli, H.B.; Shrestha, T.; Jha, D.; Shrestha, R.L.; Bhattarai, D.P. Porosity Analysis of Acacia catechu Seed-derived Carbon Materials Activated with Sodium Hydroxide and Potassium Hydroxide: Insights from Methylene Blue and Iodine Number Methods. *J. Nepal Chem. Soc.* **2025**, *45*, 57–65. [CrossRef]
29. Wang, H.; Tang, M.; Abdelaal, A.; Garah, M.E.; Jlassi, K.; Abdullah, A.M.; Chehimi, M.M. Appraisal of a Fistful of Methods for Producing Porous Biochar. *ChemRxiv* **2025**. [CrossRef]
30. Zhao, F.; Shan, R.; Li, W.; Zhang, Y.; Yuan, H.; Chen, Y. Synthesis, Characterization, and Dye Removal of $ZnCl_2$-Modified Biochar Derived from Pulp and Paper Sludge. *ACS Omega* **2021**, *6*, 34712–34723. [CrossRef]
31. Du, C.; Liu, B.; Hu, J.; Li, H. Determination of iodine number of activated carbon by the method of ultraviolet–visible spectroscopy. *Mater. Lett.* **2021**, *285*, 129137. [CrossRef]
32. Lo, M.; Tang, M.; Faye, D.; Vaiyapuri, V.; Jayaram, A.; Mani, N.; Jouini, M.; Chehimi, M.M. Silver-modified sugarcane bagasse biochar-based electrode materials for the electrochemical detection of mercury ions in aqueous media. *Electrochim. Acta* **2025**, *540*, 147214. [CrossRef]
33. Zeng, H.; Zhang, J.; Lin, L.; Liu, J.; Shi, J. Enhanced electrochemical performance of wood derived carbon-based supercapacitor electrodes by freezing and thawing pretreatment salt template method. *Ind. Crop. Prod.* **2025**, *225*, 120546. [CrossRef]
34. Umino, S.; Newman, J. Diffusion of Sulfuric Acid in Concentrated Solutions. *J. Electrochem. Soc.* **1993**, *140*, 2217–2221. [CrossRef]
35. Faye, D.; Lo, M.; Seye, D.; Diop, C.A.B.; Diop, M.G.; Ngom, A.; Dieng, M.; Bhakta, A.K.; Gningue-Sall, D.; Chehimi, M.M.; et al. Silver Nanoparticles Supported by Carbon Nanotubes Functionalized with 1,2,3-Benzenetricarboxylic Acid: Spectroscopic Analysis and Electrochemical Capacitance. *J. Inorg. Organomet. Polym. Mater.* **2025**, *35*, 7806–7819. [CrossRef]
36. Thomas, D.; Fernandez, N.B.; Mullassery, M.D.; Surya, R. Iron oxide loaded biochar/polyaniline nanocomposite: Synthesis, characterization and electrochemical analysis. *Inorg. Chem. Commun.* **2020**, *119*, 108097. [CrossRef]
37. Li, B.; Li, C.; Li, D.; Zhang, L.; Zhang, S.; Cui, Z.; Wang, D.; Tang, Y.; Hu, X. Activation of pine needles with zinc chloride: Evolution of functionalities and structures of activated carbon versus increasing temperature. *Fuel Process. Technol.* **2023**, *252*, 107987. [CrossRef]
38. Yan, L.; Liu, Y.; Zhang, Y.; Liu, S.; Wang, C.; Chen, W.; Liu, C.; Chen, Z.; Zhang, Y. ZnCl2 modified biochar derived from aerobic granular sludge for developed microporosity and enhanced adsorption to tetracycline. *Bioresour. Technol.* **2020**, *297*, 122381. [CrossRef]

39. Zhao, J.; Zhou, D.; Zhang, J.; Li, F.; Chu, G.; Wu, M.; Pan, B.; Steinberg, C.E. The contrasting role of minerals in biochars in bisphenol A and sulfamethoxazole sorption. *Chemosphere* **2021**, *264*, 128490. [CrossRef]
40. Xia, D.; Tan, F.; Zhang, C.; Jiang, X.; Chen, Z.; Li, H.; Zheng, Y.; Li, Q.; Wang, Y. ZnCl 2 -activated biochar from biogas residue facilitates aqueous As(III) removal. *Appl. Surf. Sci.* **2016**, *377*, 361–369. [CrossRef]
41. Yusuff, A.S.; Lala, M.A.; Thompson-Yusuff, K.A.; Babatunde, E.O. ZnCl2-modified eucalyptus bark biochar as adsorbent: Preparation, characterization and its application in adsorption of Cr(VI) from aqueous solutions. *S. Afr. J. Chem. Eng.* **2022**, *42*, 138–145. [CrossRef]
42. Minaei, S.; Benis, K.Z.; McPhedran, K.N.; Soltan, J. Evaluation of a ZnCl2-modified biochar derived from activated sludge biomass for adsorption of sulfamethoxazole. *Chem. Eng. Res. Des.* **2022**, *190*, 407–420. [CrossRef]
43. Wei, S.; Qin, Q.; Liu, Z. Thermal behavior analysis and reaction mechanism in the preparation of activated carbon by ZnCl2 activation of bamboo fibers. *J. Anal. Appl. Pyrolysis* **2024**, *179*, 106500. [CrossRef]
44. Smith, M.W.; Dallmeyer, I.; Johnson, T.J.; Brauer, C.S.; McEwen, J.-S.; Espinal, J.F.; Garcia-Perez, M. Structural analysis of char by Raman spectroscopy: Improving band assignments through computational calculations from first principles. *Carbon* **2016**, *100*, 678–692. [CrossRef]
45. Ayiania, M.; Weiss-Hortala, E.; Smith, M.; McEwen, J.-S.; Garcia-Perez, M. Microstructural analysis of nitrogen-doped char by Raman spectroscopy: Raman shift analysis from first principles. *Carbon* **2020**, *167*, 559–574. [CrossRef]
46. Wan, C.; Li, H.; Zhao, L.; Li, Z.; Zhang, C.; Tan, X.; Liu, X. Mechanism of removal and degradation characteristics of dicamba by biochar prepared from Fe-modified sludge. *J. Environ. Manag.* **2021**, *299*, 113602. [CrossRef]
47. Biesinger, M.C.; Lau, L.W.; Gerson, A.R.; Smart, R.S.C. Resolving surface chemical states in XPS analysis of first row transition metals, oxides and hydroxides: Sc, Ti, V, Cu and Zn. *Appl. Surf. Sci.* **2010**, *257*, 887. [CrossRef]
48. Nallayagari, A.; Sgreccia, E.; Pasquini, L.; Vacandio, F.; Kaciulis, S.; Di Vona, M.; Knauth, P. Catalytic electrodes for the oxygen reduction reaction based on co-doped (B-N, Si-N, S-N) carbon quantum dots and anion exchange ionomer. *Electrochim. Acta* **2022**, *427*, 140861. [CrossRef]
49. Syahputra, S.; Sgreccia, E.; Nallayagari, A.R.; Vacandio, F.; Kaciulis, S.; Di Vona, M.L.; Knauth, P. Influence of Nitrogen Position on the Electrocatalytic Performance of B,N-Codoped Carbon Quantum Dots for the Oxygen Reduction Reaction. *J. Electrochem. Soc.* **2024**, *171*, 066510. [CrossRef]
50. Leng, L.; Xu, S.; Liu, R.; Yu, T.; Zhuo, X.; Leng, S.; Xiong, Q.; Huang, H. Nitrogen containing functional groups of biochar: An overview. *Bioresour. Technol.* **2020**, *298*, 122286. [CrossRef]
51. Jansen, R.; van Bekkum, H. XPS of nitrogen-containing functional groups on activated carbon. *Carbon* **1995**, *33*, 1021–1027. [CrossRef]
52. Niu, Y.; Liu, Y.; Tan, H.; Xiong, Y.; Xu, T. Origination and formation of NH4Cl in biomass-fired furnace. *Fuel Process. Technol.* **2013**, *106*, 262–266. [CrossRef]
53. Shi, Q.; Zhang, X.; Shen, B.; Ren, K.; Wang, Y.; Luo, J. Enhanced elemental mercury removal via chlorine-based hierarchically porous biochar with CaCO3 as template. *Chem. Eng. J.* **2021**, *406*, 126828. [CrossRef]
54. Song, Z.; Donald, T.F.; Kirk, W.; Jia, C.Q. Electrochemical Performance of Pre-Modified Birch Biochar Monolith Supercapacitors by Ferric Chloride and Ferric Citrate. *Batteries* **2025**, *11*, 47. [CrossRef]
55. Esarev, I.V.; Agafonov, D.V.; Surovikin, Y.V.; Nesov, S.N.; Lavrenov, A.V. On the causes of non-linearity of galvanostatic charge curves of electrical double layer capacitors. *Electrochim. Acta* **2021**, *390*, 138896. [CrossRef]
56. Omidvar, M.; Dalvand, S.; Asghari, A.; Yazdanfar, N.; Sadat, H.Y.; Mohammadi, N. Fabrication of an efficient supercapacitor based on defective mesoporous carbon as electrode material utilizing Reactive Blue 15 as novel redox mediator for natural aqueous electrolyte. *Fuel* **2023**, *347*, 128472. [CrossRef]
57. Qiu, Z.; Wang, Y.; Bi, X.; Zhou, T.; Zhou, J.; Zhao, J.; Miao, Z.; Yi, W.; Fu, P.; Zhuo, S. Biochar-based carbons with hierarchical micro-meso-macro porosity for high rate and long cycle life supercapacitors. *J. Power Sources* **2018**, *376*, 82–90. [CrossRef]
58. Sánchez-Rodríguez, C.; Tovar-Martínez, E.; López-Sandoval, R. Oxidative calcination-enhanced KOH activation of d-glucose-derived carbon spheres for high microporosity in supercapacitor electrodes. *Electrochim. Acta* **2024**, *507*, 145151. [CrossRef]
59. Ouyang, Z.; Lei, Y.; Chen, Y.; Zhang, Z.; Jiang, Z.; Hu, J.; Lin, Y. Preparation and specific capacitance properties of sulfur, nitrogen co-doped graphene quantum dots. *Nanoscale Res. Lett.* **2019**, *14*, 219. [CrossRef]
60. Mousavianfard, S.A.; Molaei, A.; Manouchehri, M.; Foroozandeh, A.; Shahmohammadi, A.; Dalvand, S. Enhanced supercapacitor performance using [Caff-TEA]+[ZnBr3]$^{-}$ ionic liquid electrode in aqueous Na_2SO_4 electrolyte. *J. Energy Storage* **2025**, *109*, 115232. [CrossRef]
61. Hsia, B.; Kim, M.S.; Carraro, C.; Maboudian, R. Cycling characteristics of high energy density, electrochemically activated porous-carbon supercapacitor electrodes in aqueous electrolytes. *J. Mater. Chem. A* **2013**, *1*, 10518–10523. [CrossRef]
62. Zhu, T.; Tian, F.; Wu, J.; Li, H.; Chen, D.; Qi, R.; Niu, Y.; Zhang, F.; Yang, Z. Synthesis of various nanostructured N-doped Cu7S4 materials for aqueous supercapacitors. *Electrochim. Acta* **2024**, *511*, 145396. [CrossRef]

63. Wang, Z.; Pan, S.; Wang, B.; Qi, J.; Tang, L.; Liu, L. Asymmetric Supercapacitors Based on Co_3O_4@MnO_2@PPy Porous Pattern Core-Shell Structure Cathode Materials. *J. Electrochem. Sci. Technol.* **2021**, *12*, 346–357. [CrossRef]
64. Ye, Z.; Wang, F.; Jia, C.; Mu, K.; Yu, M.; Lv, Y.; Shao, Z. Nitrogen and oxygen-codoped carbon nanospheres for excellent specific capacitance and cyclic stability supercapacitor electrodes. *Chem. Eng. J.* **2017**, *330*, 1166–1173. [CrossRef]
65. Dong, W.; Xie, M.; Zhao, S.; Qin, Q.; Huang, F. Materials design and preparation for high energy density and high power density electrochemical supercapacitors. *Mater. Sci. Eng. R Rep.* **2022**, *152*, 100713. [CrossRef]
66. Song, Z.; Liu, W.; Xiao, P.; Zhao, Z.; Liu, G.; Qiu, J. Nano-iron oxide (Fe_2O_3)/three-dimensional graphene aerogel composite as supercapacitor electrode materials with extremely wide working potential window. *Mater. Lett.* **2015**, *145*, 44–47. [CrossRef]
67. Zeng, F.-Y.; Sui, Z.-Y.; Liu, S.; Liang, H.-P.; Zhan, H.-H.; Han, B.-H. Nitrogen-doped carbon aerogels with high surface area for supercapacitors and gas adsorption. *Mater. Today Commun.* **2018**, *16*, 1–7. [CrossRef]
68. Tafete, G.A.; Uysal, A.; Habtu, N.G.; Abera, M.K.; Yemata, T.A.; Duba, K.S.; Kinayyigit, S. Hydrother-mally synthesized nitrogen-doped hydrochar from sawdust biomass for supercapacitor electrodes. *Int. J. Electrochem. Sci.* **2024**, *19*, 100827. [CrossRef]
69. Rawat, S.; Boobalan, T.; Krishna, B.B.; Sathish, M.; Hotha, S.; Bhaskar, T. Biochar for Supercapacitor Application: A Comparative Study. *Chem.—Asian J.* **2022**, *17*, e202200982. [CrossRef]
70. Ding, M.; Ma, Z.; Su, H.; Li, Y.; Yang, K.; Dang, L.; Li, F.; Xue, B. Preparation of porous biochar and its application in supercapacitors. *New J. Chem.* **2022**, *46*, 21788–21797. [CrossRef]
71. Nirmaladevi, S.; Boopathiraja, R.; Kandasamy, S.K.; Sathishkumar, S.; Parthibavarman, M. Wood based biochar supported MnO_2 nanorods for high energy asymmetric supercapacitor applications. *Surf. Interfaces* **2021**, *27*, 101548. [CrossRef]
72. Xue, C.-F.; Lin, Y.; Zhao, W.; Wu, T.; Wei, Y.-Y.; Li, X.-H.; Yan, W.-J.; Hao, X.-G. Green preparation of high active biochar with tetra-heteroatom self-doped surface for aqueous electrochemical supercapacitor with boosted energy density. *J. Energy Storage* **2024**, *90*, 111872. [CrossRef]
73. Cheng, J.; Lu, Y.; Sun, Y.; Deng, S.; Yang, H.; Zhang, M.; Wang, C.; Yan, J. Impact of Activation Conditions on the Electrochemical Performance of Rice Straw Biochar for Supercapacitor Electrodes. *Molecules* **2025**, *30*, 632. [CrossRef] [PubMed]
74. Madhu, R.; Veeramani, V.; Chen, S.-M.; Veerakumar, P.; Liu, S.-B.; Miyamoto, N. Functional porous carbon–ZnO nanocomposites for high-performance biosensors and energy storage applications. *Phys. Chem. Chem. Phys.* **2016**, *18*, 16466–16475. [CrossRef] [PubMed]
75. Kandhasamy, N.; Ramalingam, G.; Murugadoss, G.; Kumar, M.R.; Manibalan, G.; JothiRamalingam, R.; Yadav, H.M. Copper and zinc oxide anchored silica microsphere: A superior pseudocapacitive positive electrode for aqueous supercapacitor applications. *J. Alloys Compd.* **2021**, *888*, 161489. [CrossRef]
76. Zhang, J.; Zhao, X.S. On the Configuration of Supercapacitors for Maximizing Electrochemical Performance. *ChemSusChem* **2012**, *5*, 818–884. [CrossRef]
77. Khomenko, V.; Frackowiak, E.; Béguin, F. Determination of the specific capacitance of conducting polymer/nanotubes composite electrodes using different cell configurations. *Electrochim. Acta* **2005**, *50*, 2499–2506. [CrossRef]
78. Szkoda, M.; Ilnicka, A. Enhanced electrochemical capacitance of TiO_2 nanotubes/MoSe2 composite obtained by hydrothermal route. *Appl. Surf. Sci.* **2024**, *681*, 161490. [CrossRef]